Geophysical Journal International

Geophys. J. Int. (2021) **224,** 1188–1196
Advance Access publication 2020 October 5
GJI Seismology

doi: 10.1093/gji/ggaa472

Seismic evidence for a fossil slab origin for the Isabella anomaly

Sara L. Dougherty [1], Chengxin Jiang,[2] Robert W. Clayton [1], Brandon Schmandt[3] and Steven M. Hansen[4]

[1] *Seismological Laboratory, California Institute of Technology, Pasadena, CA* 91125, *USA. E-mail: sarad@gps.caltech.edu*
[2] *Research School of Earth Sciences, The Australian National University, Canberra, ACT* 2601, *Australia*
[3] *Department of Earth and Planetary Sciences, University of New Mexico, Albuquerque, NM* 87131, *USA*
[4] *Department of Earth and Planetary Sciences, Macquarie University, North Ryde, NSW* 2109, *Australia*

Accepted 2020 September 29. Received 2020 September 27; in original form 2020 March 7

SUMMARY

A teleseismic receiver function image of a slab-like feature that extends from the Pacific coast to the foothills of the Sierra Nevada beneath central California connects the expected location of the subducted remnant of the Monterey microplate to the high-velocity Isabella anomaly in the upper mantle. The observed structure indicates that this anomaly is a relic of the subduction zone that preceded capture of the Monterey microplate by the Pacific plate and is not due to the delamination of the lithosphere beneath the Sierra Nevada Mountains, as had been previously proposed. The fossil slab connection is also supported by surface wave tomographic images. The images are derived in part from a new linear broad-band array across the western part of central California.

Key words: Body waves; Interface waves; Seismic tomography; Crustal structure; Subduction zone processes.

1 INTRODUCTION

Seismically fast bodies have been identified in the upper mantle beneath several regions of the western U.S. Many of these features are associated with active subduction of the Juan de Fuca and Gorda plates beneath Cascadia (e.g. Obrebski *et al.* 2011; Sigloch 2011; Porritt *et al.* 2014), but there exists additional anomalies whose origins are not as clear. For example, the Siletzia Curtain (Schmandt & Humphreys 2011), Wallowa (Darold & Humphreys 2013), Nevada (Roth *et al.* 2008; West *et al.* 2009) and Isabella (e.g. Jones *et al.* 1994; Wang *et al.* 2013) high-velocity bodies are all considered to be anomalous, each with an indistinct origin. Here, we focus on discerning the tectonic origin of the Isabella anomaly.

The Isabella anomaly is located in the upper mantle beneath California's southern Great Valley, a ∼100 km wide sedimentary basin (Fig. 1). Previous seismic tomography studies have identified maximum compressional and shear wave speed perturbations of ∼5 per cent and ∼6–8.5 per cent, respectively, for this high-velocity body extending from ∼70 to ∼200–300 km depth (Zandt 2003; Schmandt & Humphreys 2010; Wang *et al.* 2013; Jones *et al.* 2014). The precise dimensions and geometry of the seismically fast volume are not well-constrained by these previous studies, with some denoting a structure that dips steeply to the east (Boyd *et al.* 2004; Wang *et al.* 2013; Jones *et al.* 2014), while others identify a vertical cylinder-like structure (Zandt 2003), both of which have variable diameters. Relatively sparse station coverage in the region overlying the Isabella anomaly has led to these resolvability issues and has inhibited imaging the structural connection between the anomaly and the overlying lithosphere, which could elucidate its origin.

The two prevailing hypotheses for the tectonic origin of the Isabella anomaly attribute it to either a fossil slab fragment (e.g. Wang *et al.* 2013; see also Porritt 2013; Cox *et al.* 2016) or the foundered lithospheric root of the Sierra Nevada batholith (e.g. Frassetto *et al.* 2011; Saleeby *et al.* 2012, and references therein). In the foundering lithosphere, or delamination, hypothesis, the dense ultramafic root of the southern Sierran batholith destabilized and was removed during the last 8–10 Myr in a downwelling process that produced the Isabella anomaly (Ducea & Saleeby 1998; Zandt *et al.* 2004). Such removal of mantle lithosphere is suggested to occur based primarily on observations of anomalous crustal thickness, subsidence of a portion of the southern Great Valley basin, uplift of the Sierra Nevada (Saleeby *et al.* 2012; Levandowski & Jones 2015) and a compositional change in volcanism (Ducea & Saleeby 1998). In the fossil slab hypothesis, the partially subducted remnant of the Monterey microplate, which was captured by the Pacific plate after spreading ceased ∼19 Ma (Lonsdale 1991), is identified as the Isabella anomaly at depth. The extinct ridge segments forming the western edges of this fragment of the Farallon plate are still preserved offshore today (Lonsdale 1991) at latitudes coincident with the Isabella anomaly (Fig. 1). In addition, the variability in topography and crustal thickness that is used to suggest delamination is also demonstrated to be similar to observations in active subduction zones, supporting a fossil slab interpretation (Porritt 2013; Wang *et al.* 2013). The fossil slab hypothesis does not preclude the possibility of southern Sierran delamination, but, rather, asserts

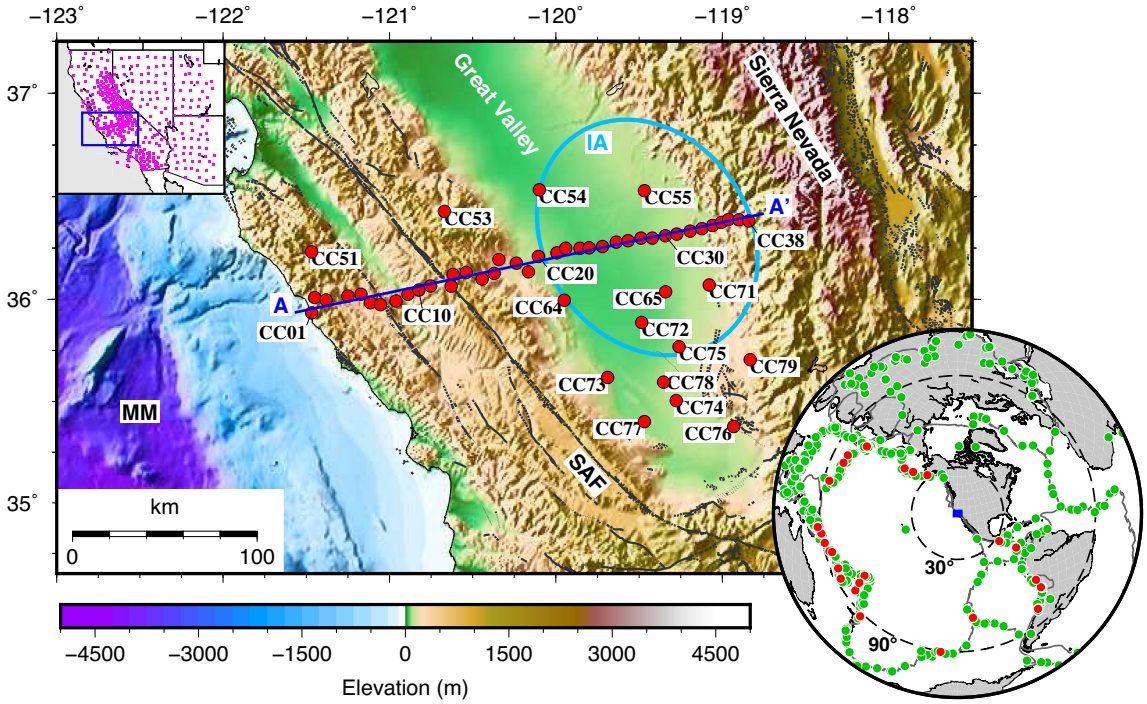

Figure 1. Topographic-bathymetric and station map. The locations of CCSE stations (red dots) and all regional broad-band stations (pink squares in top left inset) used in this study are shown. The western edge of the Monterey microplate (MM) is evident in the bathymetry. Quaternary faults, including the San Andreas Fault (SAF), are depicted by dark grey lines. The approximate boundary of the Isabella anomaly (IA) at 90 km depth from Jiang *et al.* (2018a) is indicated by the cyan ellipse. The blue line denotes the location of the 2-D profile (A-A′) in Fig. 3. Epicentral locations of teleseismic events used for the receiver function analysis (red dots; Supporting Information Table S1) and surface wave tomography (green dots; Supporting Information Data Set S1) are shown in the bottom right inset map.

that any such lithosphere foundering is not the source of the Isabella anomaly. A hybrid fossil slab and delaminated lithosphere interpretation for the tectonic origin of the Isabella anomaly has also been proposed (Bernardino *et al.* 2019). In this interpretation, the shallow, westernmost portion of the Isabella anomaly was derived from the subducted remnant of the Monterey microplate, while the eastern, deepest portion was formed by the foundered lithospheric root of the Sierra Nevada batholith (Bernardino *et al.* 2019).

The Central California Seismic Experiment (CCSE 2015) was designed to distinguish between these hypotheses through enhanced seismic imaging of the Isabella anomaly with a dense broad-band array. We employ receiver function analysis and surface wave tomography techniques to image the seismic structure of the crust and uppermost mantle beneath central California and identify the structural connection between the anomaly and the overlying lithosphere. The trajectory and strength of this connection can be used to infer the tectonic origin of the Isabella anomaly, with a shallowing eastward (i.e. towards the Sierra Nevada) trajectory suggestive of delamination and a shallowing westward (i.e. towards the Pacific coast) trajectory suggestive of a remnant slab.

2 DATA AND METHODS

The seismic data used in this study were recorded by the CCSE array and > 460 other broad-band stations which operated between 1997 and 2015 in the southwestern U.S. (Fig. 1). The CCSE array consisted of 53 broad-band seismometers which recorded data between December 2013 and October 2015. Thirty-eight of these instruments were deployed in a linear array spanning from the Pacific coast, across the Great Valley, to the Sierra Nevada foothills at an average station spacing of 7 km (Fig. 1). The remaining CCSE stations were located to the north and south of this line, primarily scattered throughout the southern Great Valley. Permanent networks (CI, BK) and other temporary arrays, such as the Sierra Nevada EarthScope Project (Gilbert *et al.* 2012; Jones *et al.* 2014), Sierra Paradox Experiment (Boyd *et al.* 2004) and EarthScope Transportable Array (TA) collected data in the broader southwestern U.S. region.

Receiver functions are generated for 61 $M_w > 6$ teleseismic earthquakes recorded by the CCSE array. These earthquakes are located at depths of 7–664 km and backazimuths of 44°–333°. Continuous noise data and a total of 777 $M_s > 5.5$ teleseismic earthquakes recorded by the broader set of stations were used by Jiang *et al.* (2018a) in ambient noise and two-plane wave tomography, respectively, to obtain Rayleigh wave phase velocities at periods of 7–100 s in a companion study to this paper. The earthquakes in this larger data set are located throughout all 360° of backazimuth (Fig. 1). Event information is taken from the Advanced National Seismic System (ANSS) Comprehensive Earthquake Catalog (ComCat) and the International Seismological Centre Bulletin event catalogue (International Seismological Centre 2015; Supporting Information Table S1 and Data Set S1).

2.1 Receiver functions

Receiver functions (RFs) are constructed using standard methods, following Ma & Clayton (2015, 2016). Three-component waveforms for each event are rotated to R-T-Z coordinates and bandpass filtered to 1–50 s. An iterative time-domain deconvolution technique (Kikuchi & Kanamori 1982; Ligorría & Ammon 1999) is

used to generate *P*-to-*S* RFs with a low-pass Gaussian filter with a parameter of 2.5 applied. This filter parameter is chosen to allow the highest frequencies (for highest resolution) that do not create significant spurious arrivals in the RFs. We perform a qualitative assessment of the results from a few different filter bands to select the filter parameter that produces the clearest signals. The corresponding cut-off frequency for the selected filter parameter is ∼1.2 Hz (Ma & Clayton 2016). The quality (A, B, C, D) of all RFs obtained for each event is assessed visually by inspecting the apparent noise, or artefact, level and only those events with the highest quality rankings (i.e. A or B) are retained for further analysis. Out of the 61 earthquakes for which RFs are generated, 31 meet these criteria (Fig. 1, Supporting Information Table S1). The RFs at the 38 CCSE stations along profile A-A′ (Fig. 1) for these 31 events are then stacked. Based on the success that Ma & Clayton (2015, 2016) found using free-surface multiples in their RF imaging along similarly dense station profiles in other regions, we explore the PpPp and PpPs phases (Fig. 2) in our RFs and also find strong signals from these multiple phases.

Common conversion point (CCP) migration (Dueker & Sheehan 1997) is performed using the PpPp phase with a bin size of 1.5 km in horizontal space and 0.1 km in depth space. A 1-D model extracted from a reference 2-D velocity model (Supporting Information Fig. S1) at each station location along A-A′ is used for the time-depth conversion. This reference model across the CCSE array is constructed from a previous compilation of seismic refraction and reflection surveys that were conducted in central California (Fliedner *et al.* 2000) and includes the low-velocity Great Valley basin, which is important for correctly migrating the RFs with depth (Dougherty *et al.* 2016). This model has been validated through 2-D waveform modelling using local earthquakes recorded by the CCSE array (Dougherty *et al.* 2016). Two alternative velocity models are also tested, with their resultant CCP migrated images exhibiting small shifts in interface depths (± ∼2–5 km), but otherwise no change in the imaged structure (Supporting Information Figs S2 and S3). A test with a 1-D global reference model (iasp91; Kennett & Engdahl 1991) illustrates the importance of including the Great Valley basin in the velocity model used for migration (Supporting Information Fig. S4). The CCP migrated images from this test depict larger shifts in interface depths (± ∼3–8 km), steepening of dipping interfaces and a loss of detail (e.g. pair of west dipping interfaces reduced to single diffuse interface) for structures beneath the Great Valley. CCP migration results from 30 events are stacked to produce the final image. One event is excluded (Supporting Information Table S1) due to low-quality results produced at several stations. A hit count cross-section is used as a resolution proxy for the CCP migrated image (Supporting Information Fig. S5). The described CCP migration procedure is repeated using the Ps (Supporting Information Fig. S6) and PpPs (Supporting Information Fig. S7) phases.

2.2 Rayleigh wave tomography

Surface wave tomography was performed in our companion study to this paper (Jiang *et al.* 2018a), with results along a new cross-section approximately coincident with RF profile A-A′ (Fig. 1) presented in this study. The techniques used to produce the tomography results shown in this study are briefly summarized here. The reader is referred to Jiang *et al.* (2018a) for further details.

For ambient noise tomography, a previous set of Rayleigh wave phase velocities generated from 2005–2007 data (Lin *et al.* 2008) was supplemented with new noise correlations between stations which operated between 1997 and 2015. The frequency–time analysis (FTAN) method (Levshin & Ritzwoller 2001) was applied to determine the phase velocities between stations. The complete set of phase velocities were then used in a ray-theory based tomographic inversion (Barmin *et al.* 2001) to generate short-period (7–25 s) Rayleigh wave phase velocity maps for the broader study region.

The FTAN method was also applied to the 777 teleseismic earthquakes that comprise the larger event data set to isolate the fundamental Rayleigh wave on each seismogram and obtain the phase and amplitude. The two-plane wave tomography method (Forsyth & Li 2005; Yang & Forsyth 2006) was then used to invert this phase and amplitude information for 25–100 s period regional Rayleigh wave phase velocity maps. This inversion was performed using the 2-D finite-frequency sensitivity kernels of Zhou *et al.* (2004).

The 7–100 s phase velocity dispersion curves for 1-D shear wave velocity (Vs) were inverted using a Bayesian Markov chain Monte Carlo method (Shen *et al.* 2013) on a $0.2^\circ \times 0.2^\circ$ grid. The three main steps to this Vs inversion include (1) the determination of parameters to represent the model space, (2) the generation of a Markov chain of candidate models and (3) a χ^2 misfit evaluation. The model space consisted of a set of 1-D Vs profiles from 0 to 250 km depth at all grid points, which were then assembled into a 3-D Vs model after running up to 300 000 iterations.

3 RESULTS

3.1 Receiver functions

The stacked RFs and final CCP migration image both exhibit a high level of interpretable detail (Fig. 3). In this study, we focus on the dominant signals from the basin, Moho and dipping structures.

Prominent reverberations within the Great Valley basin can be observed in the stacked RFs at stations CC14 through CC31 and are strongest in the deepest part of the basin (Fig. 3). Sedimentary basins are known to produce such reverberations due to the high-velocity contrast between the sediments and underlying basement rocks (or within sedimentary layers themselves) and the laterally varying basin geometry (e.g. Zelt & Ellis 1999; Zhu & Kanamori 2000; Yu *et al.* 2015). The low-amplitude, broader and/or delayed direct *P* arrivals at these stations (Fig. 3) can also be attributed to basin effects wherein either the direct *P* phase is masked by the reverberations (Yu *et al.* 2015) or the reverberations arrive shortly after direct *P*, limiting its resolvability (Cassidy 1992; Zelt & Ellis 1999). Similarly, basin reverberations can also interfere with and obscure subtler phases associated with deeper structure, such as the Moho (e.g. Zelt & Ellis 1999; Zheng *et al.* 2005; Li *et al.* 2007). The PpPs phase converted from the basement underlying the basin can be identified amidst the other basin multiples in Fig. 3.

The Ps phase generated at the Moho is visible only from the coast to the San Andreas Fault (SAF) and beneath the Sierra Nevadan foothills in the stacked RF profile (Fig. 3). It is notably missing beneath the Great Valley, likely due to the effects of basin reverberations noted above and/or a weak velocity contrast caused by a high-velocity lower crust. This absence of the Moho Ps phase beneath the Great Valley was also noted by Zandt *et al.* (2004). The Moho Ps phase is observed to arrive earlier in the west (∼3–4 s) and later in the east (∼4–6 s), suggesting a west to east deepening of the Moho along the profile. This is consistent with previous findings in central California of a shallower Moho in the west and a deeper Moho beneath the Sierran foothills (e.g. Colburn & Mooney 1986;

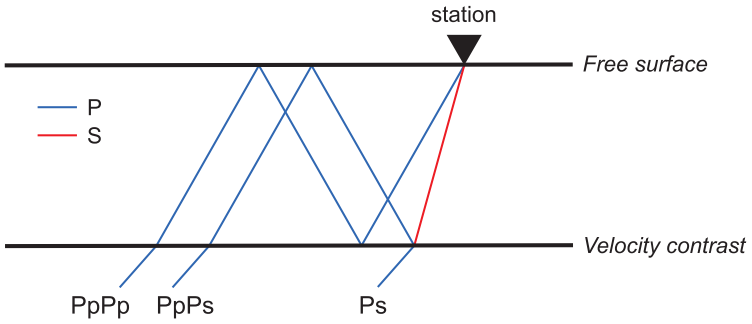

Figure 2. Ray path schematic. Ps, PpPp and PpPs phases arriving at a single three-component station are illustrated.

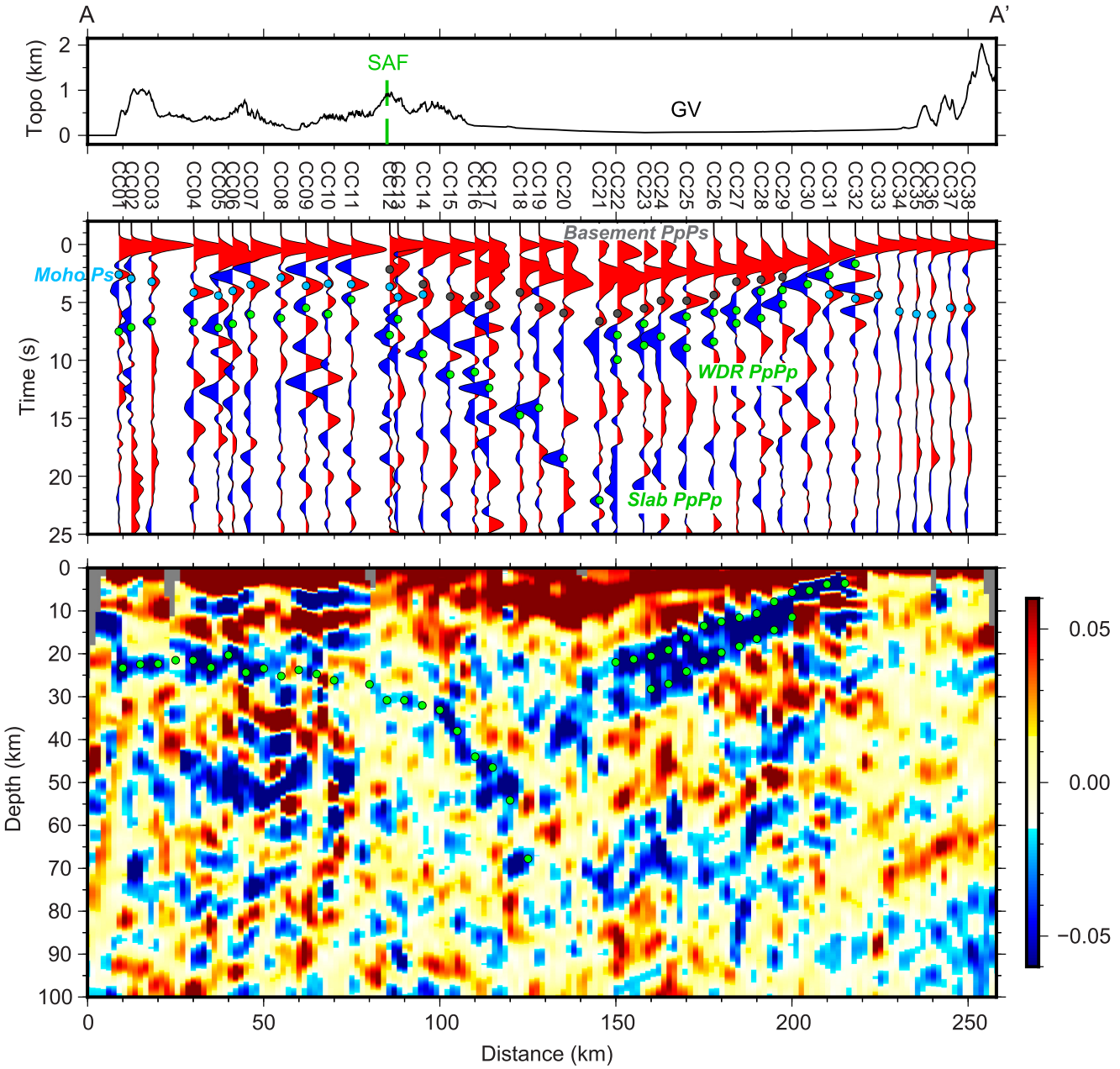

Figure 3. Receiver function profile. Top: topography along profile A-A′ in Fig. 1. SAF: San Andreas Fault; GV: Great Valley. Middle: stacked receiver functions for 31 events (Supporting Information Table S1) recorded at the 38 CCSE stations located along the profile (Fig. 1). Basement PpPs (dark grey dots), Moho Ps (cyan dots), slab PpPp and west dipping reflector (WDR) PpPp (green dots) phases are indicated. See the text for details. Bottom: CCP migration of the PpPp phase. Green dots delineate the inferred slab and WDR structures.

Fliedner *et al.* 2000; Frassetto *et al.* 2011). A Moho converted arrival is unclear in the PpPp CCP migrated image (Fig. 3).

A negative polarity PpPp phase delineates a continuous structure that is nearly horizontal between the coast and the SAF at ∼20–25 km depth before dipping eastward at ∼60° beneath the Great Valley down to ∼70 km depth (Fig. 3). This structure can be observed in both the straight RFs and the CCP migrated image, but the PpPp signal is strongest in the CCP results. We interpret this signal to be representative of a slab-like structure. It is important to note here that due to the polarity change that occurs at the free surface for the P wave reflection, the PpPp phase is generally negative in RFs for an interface with increasing velocity, or positive impedance contrast, downward (Li *et al.* 2007; Tonegawa *et al.* 2013). Further details on our converted phase identification are provided in the supplemental document.

Beneath the eastern Great Valley, a pair of very strong subparallel PpPp arrivals can be seen within the crust in both the stacked RF and CCP images (Fig. 3). These west dipping discontinuities, or reflectors, begin near the surface at the easternmost edge of the valley and reach a maximum depth of ∼28 km at a point about 70 km to the west. The location, geometry and strength of these interfaces suggest that they correspond to a pair of structures that were previously identified in a seismic reflection survey across the eastern Great Valley (Supporting Information Fig. S8; Wentworth *et al.* 1987; Miller & Mooney 1994).

3.2 Rayleigh wave tomography

In our Rayleigh wave tomography model, the Isabella anomaly is imaged as a subhorizontal body between ∼50 and ∼90 km depth west of the SAF (Fig. 4). East of the SAF, the anomaly dips rather steeply eastward beneath the Great Valley and Sierra Nevada foothills down to ∼150 km depth. This depiction of the Isabella anomaly represents the eastern continuation of the slab structure identified from the RFs. In the uppermost mantle, the anomaly is dominated by Vs values of 4.4–4.55 km s^{-1}, exhibiting a peak Vs perturbation of ∼6 per cent relative to the regional average across the entire model area (Fig. 4). The observed steep easterly dip and peak Vs perturbation are consistent with findings from some previous relatively low-resolution (compared to this study) seismic imaging studies of the Isabella anomaly (Boyd *et al.* 2004; Wang *et al.* 2013; Jones *et al.* 2014). However, the clear, nearly horizontal westward extension of the anomaly towards the coast was not present in any of the earlier studies, except for Jiang *et al.* (2018a).

In both map view and cross-section, the top ∼30–40 km of the imaged Isabella anomaly is located more than 50 km west of the Sierra Nevada with no visible connection to this topographic high (Fig. 4). Slow lower crust observed beneath the Sierra Nevada (Fig. 4), however, is suggested by Jiang *et al.* (2018a) to indicate a possible localized lithosphere foundering event that is not connected to the Isabella anomaly. This inference is made from their joint Rayleigh and S wave tomographic inversion in a companion study to this paper.

4 DISCUSSION

4.1 Remnant monterey slab

The stacked RFs, CCP migrated image and Rayleigh wave tomographic model all clearly show the Isabella high-velocity anomaly is an east dipping body which is connected to a structure that extends westward to the Pacific coast. We interpret this structure as the remnant slab of the Monterey microplate. This interpretation is consistent with the results of some recent seismic imaging studies (Wang *et al.* 2013; see also Porritt 2013; Cox *et al.* 2016; Jiang *et al.* 2018a; Schardong *et al.* 2019) and geodynamic modelling of along strike slab translation by Pikser *et al.* (2012). The lack of an eastward trajectory towards the Sierra Nevada for the structural connection between the Isabella anomaly and overlying lithosphere, coupled with the anomaly's imaged location well west of the Sierra Nevada, argues against the delamination, or foundered lithospheric root, hypothesis for the origin of this anomaly (e.g. Frassetto *et al.* 2011; Saleeby *et al.* 2012, and references therein). However, a hybrid origin with a Monterey slab remnant and delaminating lithosphere beneath the Sierra Nevada batholith cannot be ruled out (Bernardino *et al.* 2019).

The main criticism of the fossil slab hypothesis focuses on the question of whether a remnant subducted plate could remain attached and intact while being translated hundreds of kilometres along strike after being captured by the Pacific plate when subduction ceased in the Miocene (Nicholson *et al.* 1994). There are several lines of evidence which provide support for both the feasibility of this scenario and the present-day existence of a remnant Monterey slab at a location coincident with the Isabella anomaly. 3-D geodynamic models of fluid flow are able to reproduce the lateral translation of the Monterey slab beneath North America and demonstrate that the persistence of the slab, without significant deformation, is physically feasible (Pikser *et al.* 2012). The oceanic crust of the Monterey microplate in its current position has also been traced from the fossil trench landward, at least as far east as the SAF, using seismic refraction and reflection (Miller *et al.* 1992; Brocher *et al.* 1999; and references therein). Along the creeping section of the SAF overlying the remnant Monterey slab, a deficit in the water budget necessary for the serpentinization of rocks along the fault, which is believed to be responsible for the observed aseismic creep and anomalously low shear stress (e.g. Hickman & Zoback 2004; Moore & Rymer 2007, and references therein), could be satisfied with water produced from dehydration of the slab (Pikser *et al.* 2012) and/or the overlying mantle wedge (Kirby *et al.* 2014). Similarly, an isolated group of non-volcanic tremor sources offset 10 km eastward from the creeping SAF segment at nearly 30 km depth suggests the presence of the fossil slab at the base of the crust, which may provide a fluid source for tremor production (Shelly 2015). Teleseismic shear wave splitting parameters measured along the CCSE also reveal anomalous nearly fault-parallel anisotropy in the lithosphere within a ∼50 km wide zone east of the SAF, coincident with the location of the Isabella anomaly (Jiang *et al.* 2018b). This zone of margin-parallel shear in the uppermost mantle may be explained by the translation of the fossil Monterey slab fragment with the Pacific plate (Jiang *et al.* 2018b).

A lateral offset in the depicted location of the remnant slab in the Rayleigh wave tomography model (Fig. 4) relative to the CCP migrated image (Fig. 3) may also raise questions (Supporting Information Fig. S9), and we propose a few possible explanations. It is widely recognized that surface wave tomography tends to smear velocity anomalies laterally (e.g. Levandowski & Jones 2015) and suffer from increasingly poor lateral resolution with depth (e.g. Jones *et al.* 2014). Such smearing and resolution effects may combine to produce what can be considered a low-frequency representation of the slab in our Rayleigh wave tomography model. Jiang *et al.* (2018a) conducted synthetic testing of the surface wave inversion methods employed to produce the results shown in this study for a dipping slab and found poor resolution, which makes it difficult to ascertain the true geometry of the slab, including

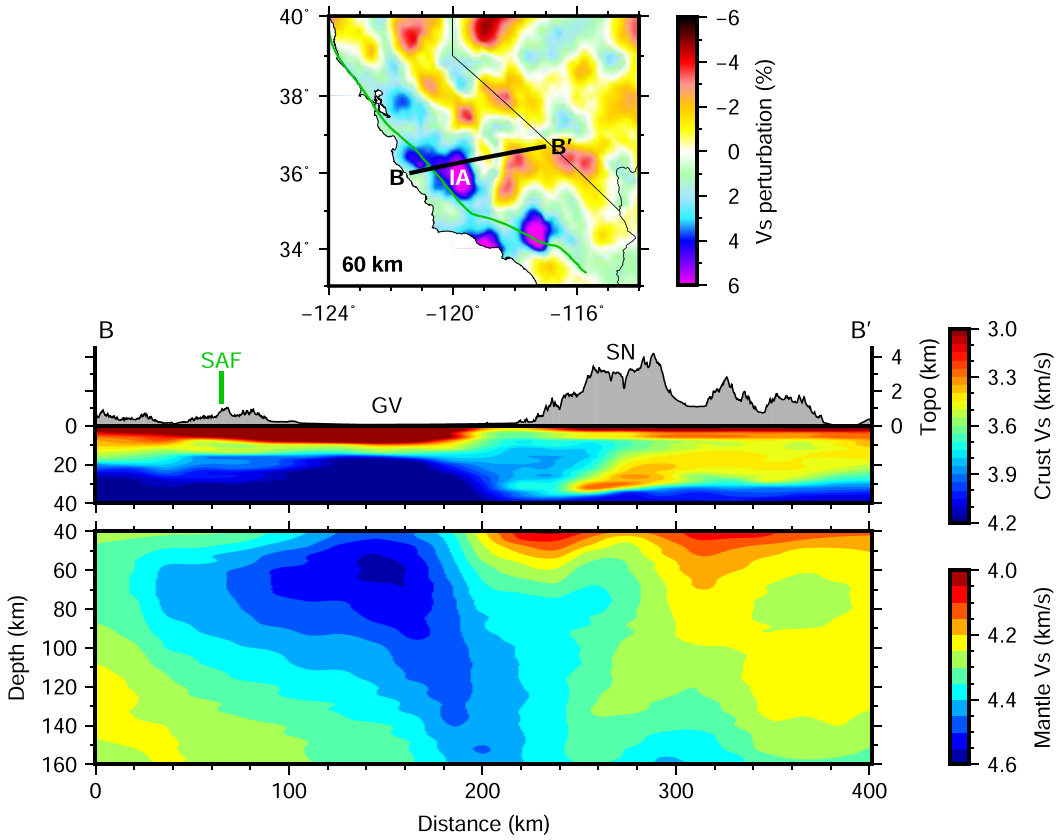

Figure 4. Rayleigh wave tomography. Top: map of Vs at 60 km depth plotted as perturbations relative to the regional average across the entire model area. The locations of the 2-D cross-section (B-B′; black line), San Andreas Fault (SAF; green line) and Isabella anomaly (IA) are indicated. Bottom: cross-section of topography and absolute Vs in the crust and mantle along profile B-B′. Note the different colour bars for each compositional layer of the model. Zero kilometre distance corresponds to ∼19 km along profile A-A′ (Fig. 3). GV: Great Valley; SN: Sierra Nevada.

the precise location of the bend from nearly horizontal to steeply dipping. These difficulties related to resolvability could produce the observed discrepancies between our Rayleigh wave tomography and CCP migrated images. An inherent inability to precisely resolve the thickness of the slab with tomographic methods may provide additional freedom to connect the upper boundary of the slab as defined in the CCP migrated image to that in the tomography model. The choice of parameters used in the tomographic inversion also has an effect on controlling the position of the slab (see, e.g. Rawlinson & Spakman 2016). For comparison, similar discrepancies between surface wave tomography (e.g. Obrebski *et al.* 2011) and RF (e.g. Bostock *et al.* 2002) images can also be observed in the Cascadia subduction zone, where the lateral offset in the depicted location of the Juan de Fuca slab is 50–75 km or more.

4.2 West dipping reflections

A pair of nearly parallel west dipping interfaces within the crust beneath the eastern Great Valley are prominent features in both the stacked RFs and the CCP migrated image (Fig. 3). These features are not the main target of this study and warrant further in-depth analysis, but are discussed briefly here due to their prominence in our results.

A seismic reflection survey across the eastern Great Valley to the Sierra Nevadan foothills imaged a pair of strong subparallel reflectors dipping ∼30°–35° W through the mid-crust (Supporting Information Fig. S8), separated by ∼7–8 km (Zoback & Wentworth 1986; Wentworth *et al.* 1987; Miller & Mooney 1994). The location and geometry of these reflectors is consistent with the west dipping interfaces evident in our receiver function images. The interpretation of these features is challenging because (1) this region has experienced a complex geologic history that is still debated (Shervais *et al.* 2004; Dickinson 2008) and (2) the basement structure is obscured by Great Valley sediments. Seismic, gravity and magnetic observations have been used to suggest that the Great Valley is underlain by a large ophiolite body that was emplaced in the Mesozoic (e.g. Godfrey & Klemperer 1998). However, Dickinson (2008) suggests that this region represents a long-lived subduction complex that includes ophiolite fragments, analogous to the Kings-Kaweah belt which outcrops in the Sierra Nevadan foothills and predates the Franciscan Complex of the Coast Range. Crustal shortening occurred as oceanic material accreted onto the continental margin along west dipping thrust faults (Schweickert *et al.* 1984). Remnants of these thrust faults are proposed as one possible explanation for the observed reflections (Zoback & Wentworth 1986; Wentworth *et al.* 1987). An alternative interpretation attributes the west dipping reflections to either major shear zones formed during accretion or synbatholithic ductile shear zones that accommodated crustal extension during intrusion of the Sierra Nevada batholith (Miller & Mooney 1994). Miller & Mooney (1994) further reconciled these two possibilities by suggesting that Nevadan Orogeny shear zones acted as lines of weakness along which extension related to batholithic intrusion was later accommodated. Discerning

the most likely cause of the observed west dipping reflectors, or interfaces, is beyond the scope of this study.

5 CONCLUSIONS

The CCSE enabled high-resolution seismic imaging of the Isabella anomaly in the upper mantle beneath central California, which clearly depicts the structural connection between this anomaly and the overlying lithosphere for the first time. The top of the Isabella anomaly is found to project westwards toward the coast at a nearly horizontal orientation. We interpret this structure as indicative of a fossil slab origin for the anomaly, attributed to the partially subducted remnant of the Monterey microplate.

Prominent west dipping crustal interfaces beneath the eastern Great Valley basin are also evident in our receiver function imaging and correlate with a pair of subparallel reflectors observed in prior active source reflection imaging. These features warrant further investigation to determine their tectonic origin.

ACKNOWLEDGEMENTS

Seismic waveform data from the CCSE array (CCSE, doi: 10.7909/C3B56GVW) and other broad-band networks used in this study are available from the Incorporated Research Institutions for Seismology Data Management Center. Earthquake catalogue data were obtained from the Advanced National Seismic System Comprehensive Earthquake Catalog and the International Seismological Centre Bulletin event catalogue and are provided in the Supporting Information. We are grateful to Richard Guy and Charles Hoots for their work installing the CCSE array. We thank the Gordon and Betty Moore Foundation through the Tectonics Observatory at Caltech for the use of the instruments. We also thank Editor Ana Ferreira, Robert Porritt and an anonymous reviewer for helpful comments which improved the manuscript. This research was supported by NSF EAR-1314910 and EAR-1315856.

REFERENCES

Barmin, M.P., Ritzwoller, M.H. & Levshin, A.L., 2001. A fast and reliable method for surface wave tomography, *Pure appl. Geophys.,* **158**(8), 1351–1375.

Bernardino, M.V., Jones, C.H., Levandowski, W., Bastow, I., Owens, T.J. & Gilbert, H., 2019. A multicomponent Isabella anomaly: resolving the physical state of the Sierra Nevada upper mantle from Vp/Vs anisotropy tomography, *Geosphere,* **15**(6), 2018–2042.

Bostock, M.G., Hyndman, R.D., Rondenay, S. & Peacock, S.M., 2002. An inverted continental Moho and serpentinization of the forearc mantle, *Nature,* **417,** 536–538.

Boyd, O.S., Jones, C.H. & Sheehan, A.F., 2004. Foundering lithosphere imaged beneath the southern Sierra Nevada, California, USA, *Science,* **305,** 660–662.

Brocher, T.M. & Abramovitz, T., U. S. ten Brink, 1999. Synthesis of crustal seismic structure and implications for the concept of a slab gap beneath coastal California, *Int. Geol. Rev.,* **41**(3), 263–274.

Cassidy, J.F., 1992. Numerical experiments in broadband receiver function analysis, *Bull. seism. Soc. Am.,* **82**(3), 1453–1474.

CCSE, 2015. *Central California Seismic Experiment,* Caltech, dataset, doi:10.7909/C3B56GVW.

Colburn, R.H. & Mooney, W.D., 1986. Two-dimensional velocity structure along the synclinal axis of the Great Valley, California, *Bull. seism. Soc. Am.,* **76**(5), 1305–1322.

Cox, P., Stubailo, I. & Davis, P., 2016. Receiver function and geometric tomography along the Monterey microplate to test slab delamination or lithospheric drip models of the Isabella anomaly, California, *Bull. seism. Soc. Am.,* **106**(1), 267–280.

Darold, A. & Humphreys, E., 2013. Upper mantle seismic structure beneath the Pacific Northwest: a plume-triggered delamination origin for the Columbia River flood basalt eruptions, *Earth planet. Sci. Lett.,* **365,** 232–242.

Dickinson, W.R., 2008. Accretionary Mesozoic-Cenozoic expansion of the Cordilleran continental margin in California and adjacent Oregon, *Geosphere,* **4**(2), 329–353.

Dougherty, S.L., Hoots, C.R., Hansen, S., Schmandt, B. & Clayton, R.W., 2016. Seismic structure beneath the Great Valley, central California: implications for the tectonic origin of the Isabella anomaly, *Seismol. Res. Lett.,* **87**(2B), 512, doi:10.1785/0220160046.

Ducea, M. & Saleeby, J., 1998. A case for delamination of the deep batholithic crust beneath the Sierra Nevada, California, *Int. Geol. Rev.,* **40,** 78–93.

Dueker, K.G. & Sheehan, A.F., 1997. Mantle discontinuity structure from midpoint stacks of converted *P* to *S* waves across the Yellowstone hotspot track, *J. geophys. Res.,* **102,** 8313–8327.

Fliedner, M.M., Klemperer, S.L. & Christensen, N.I., 2000. Three-dimensional seismic model of the Sierra Nevada arc, California, and its implications for crustal and upper mantle composition, *J. geophys. Res.,* **105**(B5), 10 899–10 921.

Forsyth, D.W. & Li, A., 2005. Array analysis of two-dimensional variations in surface wave phase velocity and azimuthal anisotropy in the presence of multipathing interference, in *Seismic Earth: Array Analysis of Broadband Seismograms, Geophysical Monograph Series,* Vol. 157, pp. 81–97, eds, Levander, A. & Nolet, G., AGU.

Frassetto, A.M., Zandt, G., Gilbert, H., Owens, T.J. & Jones, C.H., 2011. Structure of the Sierra Nevada from receiver functions and implications for lithospheric foundering, *Geosphere,* **7**(4), 898–921.

Gilbert, H., Yang, Y., Forsyth, D.W., Jones, C.H., Owens, T.J., Zandt, G. & Stachnik, J.C., 2012. Imaging lithospheric foundering in the structure of the Sierra Nevada, *Geosphere,* **8**(6), 1310–1330.

Godfrey, N.J. & Klemperer, S.L., 1998. Ophiolitic basement to a forearc basin and implications for continental growth: the Coast Range/Great Valley ophiolite, California, *Tectonics,* **17**(4), 558–570.

Hickman, S. & Zoback, M., 2004. Stress orientations and magnitudes in the SAFOD pilot hole, *Geophys. Res. Lett.,* **31,** L15S12, doi:10.1029/2004GL020043.

International Seismological Centre, 2015,. *On-line Bulletin,* http://www.isc.ac.uk, International Seismological Centre.

Jiang, C., Schmandt, B., Hansen, S.M., Dougherty, S.L., Clayton, R.W., Farrell, J. & Lin, F.-C., 2018a. Rayleigh and *S* wave tomography constraints on subduction termination and lithospheric foundering in central California, *Earth planet. Sci. Lett.,* **488,** 14–26.

Jiang, C., Schmandt, B. & Clayton, R.W., 2018b. An anisotropic contrast in the lithosphere across the central San Andreas Fault, *Geophys. Res. Lett.,* **45,** doi:10.1029/2018GL077476.

Jones, C.H., Kanamori, H. & Roecker, S.W., 1994. Missing roots and mantle "drips": regional Pn and teleseismic arrival times in the southern Sierra Nevada and vicinity, California, *J. geophys. Res.,* **99,** 4567–4601.

Jones, C.H., Reeg, H., Zandt, G., Gilbert, H., Owens, T.J. & Stachnik, J., 2014. *P*-wave tomography of potential convective downwellings and their source regions, Sierra Nevada, California, *Geosphere,* **10**(3), 505–533.

Kennett, B.L.N. & Engdahl, E.R., 1991. Traveltimes for global earthquake location and phase identification, *Geophys. J. Int.,* **105**(2), 429–465.

Kikuchi, M. & Kanamori, H., 1982. Inversion of complex body waves, *Bull. seism. Soc. Am.,* **72**(2), 491–506.

Kirby, S.H., Wang, K. & Brocher, T.M., 2014. A large mantle water source for the northern San Andreas fault system: a ghost of subduction past, *Earth Planets Space,* **66,** doi:10.1186/1880-5981-66-67.

Levandowski, W. & Jones, C.H., 2015. Linking Sierra Nevada, California, uplift to subsidence of the Tulare basin using a seismically derived density model, *Tectonics,* **34,** doi:10.1002/2015TC003824.

Levshin, A.L. & Ritzwoller, M.H., 2001. Automated detection, extraction, and measurement of regional surface waves, *Pure appl. Geophys.,* **158**(8), 1531–1545.

Li, J., Tian, B., Wang, W., Zhao, L. & Yao, Z., 2007. Lateral variation in the sedimentary structure of west Bohai Bay Basin inferred from P-multiple receiver functions, *Bull. seism. Soc. Am.,* **97**(4), 1355–1363.

Ligorría, J.P. & Ammon, C.J., 1999. Iterative deconvolution and receiver-function estimation, *Bull. seism. Soc. Am.,* **89**(5), 1395–1400.

Lin, F.-C., Moschetti, M.P. & Ritzwoller, M.H., 2008. Surface wave tomography of the western United States from ambient seismic noise: Rayleigh and Love wave phase velocity maps, *Geophys. J. Int.,* **173**(1), 281–298.

Lonsdale, P., 1991. Structural patterns of the Pacific floor offshore of peninsular California, in *The Gulf and Peninsular Province of the Californias, AAPG Memoir,* Vol. 47, pp. 87–125, eds, Dauphin, J.P. & Simoneit, B.R.T., AAPG.

Ma, Y. & Clayton, R.W., 2015. Flat slab deformation caused by interplate suction force, *Geophys. Res. Lett.,* **42,** doi:10.1002/2015GL065195.

Ma, Y. & Clayton, R.W., 2016. Structure of the Los Angeles Basin from ambient noise and receiver functions, *Geophys. J. Int.,* **206,** 1645–1651.

Miller, K.C. & Mooney, W.D., 1994. Crustal structure and composition of the southern Foothills Metamorphic Belt, Sierra Nevada, California, from seismic data, *J. geophys. Res.,* **99,** 6865–6880.

Miller, K.C., Howie, J.M. & Ruppert, S.D., 1992. Shortening within underplated oceanic crust beneath the central California margin, *J. geophys. Res.,* **97,** 19 961–19 980.

Moore, D.E. & Rymer, M.J., 2007. Talc-bearing serpentinite and the creeping section of the San Andreas fault, *Nature,* **448,** 795–797.

Nicholson, C., Sorlien, C.C., Atwater, T., Crowell, J.C. & Luyendyk, B.P., 1994. Microplate capture, rotation of the western Transverse Ranges, and initiation of the San Andreas transform as a low-angle fault system, *Geology,* **22,** 491–495.

Obrebski, M., Allen, R.M., Pollitz, F. & Hung, S.-H., 2011. Lithosphere-asthenosphere interaction beneath the western United States from the joint inversion of body-wave traveltimes and surface-wave phase velocities, *Geophys. J. Int.,* **185**(2), 1003–1021.

Pikser, J.E., Forsyth, D.W. & Hirth, G., 2012. Along-strike translation of a fossil slab, *Earth planet. Sci. Lett.,* **331–332,** 315–321.

Porritt, R.W., 2013. Tracing the Farallon plate through seismic imaging with USArray, *Doctoral dissertation*, University of California, Berkeley.

Porritt, R.W., Allen, R.M. & Pollitz, F.F., 2014. Seismic imaging east of the Rocky Mountains with USArray, *Earth planet. Sci. Lett.,* **402,** 16–25.

Rawlinson, N. & Spakman, W., 2016. On the use of sensitivity tests in seismic tomography, *Geophys. J. Int.,* **205**(2), 1221–1243.

Roth, J.B., Fouch, M.J., James, D.E. & Carlson, R.W., 2008. Three-dimensional seismic velocity structure of the northwestern United States, *Geophys. Res. Lett.,* **35,** L15304, doi:10.1029/2008GL034669.

Saleeby, J., Le Pourhiet, L., Saleeby, Z. & Gurnis, M., 2012. Epeirogenic transients related to mantle lithosphere removal in the southern Sierra Nevada region, California, part I: implications of thermomechanical modeling, *Geosphere,* **8**(6), 1286–1309.

Schardong, L., Ferreira, A.M.G., Berbellini, A. & Sturgeon, W., 2019. The anatomy of uppermost mantle shear-wave speed anomalies in the western U.S. from surface-wave amplification, *Earth planet Sci. Lett.,* **528,** 115822, doi:10.1016/j.epsl.2019.115822.

Schmandt, B. & Humphreys, E., 2010. Seismic heterogeneity and small-scale convection in the southern California upper mantle, *Geochem. Geophys. Geosyst.,* **11,** Q05004, doi:10.1029/2010GC003042.

Schmandt, B. & Humphreys, E., 2011. Seismically imaged relict slab from the 55 Ma Siletzia accretion to the northwest United States, *Geology,* **39**(2), 175–178.

Schweickert, R.A., Bogen, N.L., Girty, G.H., Hanson, R.E. & Merguerian, C., 1984. Timing and structural expression of the Nevadan orogeny, Sierra Nevada, California, *Bull. geol. Soc. Am.,* **95,** 967–979.

Shelly, D.R., 2015. Complexity of the deep San Andres Fault zone defined by cascading tremor, *Nat. Geosci.,* **8,** 145–151.

Shen, W., Ritzwoller, M.H., Schulte-Pelkum, V. & Lin, F.-C., 2013. Joint inversion of surface wave dispersion and receiver functions: a Bayesian Monte-Carlo approach, *Geophys. J. Int.,* **192**(2), 807–836.

Shervais, J.W., Kimbrough, D.L., Renne, P., Hanan, B.B., Murchey, B., Snow, C.A., Zoglman Schuman, M.M. & Beaman, J., 2004. Multi-stage origin of the Coast Range ophiolite, California: implications for the life cycle of supra-subduction zone ophiolites, *Int. Geol. Rev.,* **46**(4), 289–315.

Sigloch, K., 2011. Mantle provinces under North America from multifrequency *P* wave tomography, *Geochem. Geophys. Geosyst.,* **12,** Q02W08, doi:10.1029/2010GC003421.

Tonegawa, T., Iritani, R. & Kawakatsu, H., 2013. Extraction of Moho-generated phases from vertical and radial receiver functions of a seismic array, *Bull. seism. Soc. Am.,* **103**(3), 2011–2024.

Wang, Y., Forsyth, D.W., Rau, C.J., Carriero, N., Schmandt, B., Gaherty, J.B. & Savage, B., 2013. Fossil slabs attached to unsubducted fragments of the Farallon plate, *Proc. Natl. Acad. Sci. USA,* **110**(14), 5342–5346.

Wentworth, C.M., Zoback, M.D., Griscom, A., Jachens, R.C. & Mooney, W.D., 1987. A transect across the Mesozoic accretionary margin of central California, *Geophys. J. R. astr. Soc.,* **89,** 105–110.

West, J.D., Fouch, M.J., Roth, J.B. & Elkins-Tanton, L.T., 2009. Vertical mantle flow associated with a lithospheric drip beneath the Great Basin, *Nat. Geosci.,* **2,** 439–444.

Yang, Y. & Forsyth, D.W., 2006. Regional tomographic inversion of the amplitude and phase of Rayleigh waves with 2-D sensitivity kernels, *Geophys. J. Int.,* **166**(3), 1148–1160.

Yu, Y., Song, J., Liu, K.H. & Gao, S.S., 2015. Determining crustal structure beneath seismic stations overlying a low-velocity sedimentary layer using receiver functions, *J. geophys. Res.,* **120,** 3208–3218.

Zandt, G., 2003. The southern Sierra Nevada drip and the mantle wind direction beneath the southwestern United States, *Int. Geol. Rev.,* **45,** 213–224.

Zandt, G., Gilbert, H., Owens, T.J., Ducea, M., Saleeby, J. & Jones, C.H., 2004. Active foundering of a continental arc root beneath the southern Sierra Nevada in California, *Nature,* **431,** 41–46.

Zelt, B.C. & Ellis, R.M., 1999. Receiver-function studies in the Trans-Hudson Orogen, Saskatchewan, *Can. J. Earth Sci.,* **36,** 585–603.

Zheng, T., Zhao, L. & Chen, L., 2005. A detailed receiver function image of the sedimentary structure in the Bohai Bay Basin, *Phys. earth planet. Inter.,* **152,** 129–143.

Zhou, Y., Dahlen, F.A. & Nolet, G., 2004. Three-dimensional sensitivity kernels for surface wave observables, *Geophys. J. Int.,* **158**(1), 142–168.

Zhu, L. & Kanamori, H., 2000. Moho depth variation in southern California from teleseismic receiver functions, *J. geophys. Res.,* **105,** 2969–2980.

Zoback, M.D. & Wentworth, C.M., 1986. Crustal studies in central California using an 800-channel seismic reflection recording system, in *Reflection Seismology: A Global Perspective, Geodynamics Series,* Vol. 13, pp. 183–196, eds, Barazangi, M. & Brown, L., AGU.

SUPPORTING INFORMATION

Supplementary data are available at *GJI* online.

Figure S1. 2-D velocity model of the upper 45 km lithosphere structure in central California along a W–E profile across the CCSE array (CCSE 2015) from the coast (inverted triangle) to the Sierra foothills. (a) *P*-wave velocities and general structural geometries are simplified and modified from Fliedner *et al.* (2000). (b) *S*-wave velocities are estimated using a Vp/Vs ratio of 1.73. The mantle half-space is extended to 100 km depth to perform the time–depth conversion in the CCP migration. Locations of the San Andreas Fault (SAF) and Great Valley (GV) basin are indicated for reference.
Figure S2. Top: topography along profile A-A′ in Fig. 1. SAF: San Andreas Fault; GV: Great Valley. Middle: CCP migration of the PpPp phase using (bottom) an alternative 2-D velocity model of the upper 100 km lithosphere structure in central California which includes a high-velocity wedge of material beneath the eastern Great Valley. *P*-wave velocities and general structural geometries are simplified and modified from Fliedner *et al.* (2000). Green dots delineating the inferred slab and west dipping reflector structures from the CCP migration in Fig. 3 using our preferred velocity model

(Fig. S1) are shown for reference. Note the slight deepening of interfaces beneath the eastern Great Valley in this CCP image.

Figure S3. Top: topography along profile A-A′ in Fig. 1. SAF: San Andreas Fault; GV: Great Valley. Middle: CCP migration of the PpPp phase using (bottom) an alternative 2-D velocity model of the upper 100 km lithosphere structure in central California which includes a high-velocity body in the upper mantle and a general shallow basin structure. Model is derived from Rayleigh wave tomography. *P*-wave velocities are estimated using a Vp/Vs ratio of 1.73. Green dots delineating the inferred slab and west dipping reflector structures from the CCP migration in Fig. 3 using our preferred velocity model (Fig. S1) are shown for reference. Note interface depths are several kilometers shallower in this CCP image.

Figure S4. Top: topography along profile A-A′ in Fig. 1. SAF: San Andreas Fault; GV: Great Valley. Middle: CCP migration of the PpPp phase using (bottom) iasp91 1-D global reference model (Kennett & Engdahl 1991). Green dots delineating the inferred slab and west dipping reflector structures from the CCP migration in Fig. 3 using our preferred velocity model (Fig. S1) are shown for reference. Note, beneath the Great Valley, interface depths are several kilometers deeper, the dip of the inferred slab interface is significantly steeper below ∼40 km depth, and there are no longer two clear west dipping reflector structures in this CCP image.

Figure S5. Top: topography along profile A-A′ in Fig. 1. SAF: San Andreas Fault; GV: Great Valley. Bottom: Hit count cross-section for CCP migration of the PpPp phase using our preferred 2-D velocity model (Fig. S1). Black circles delineating the inferred slab and west dipping reflector structures from Fig. 3 are shown for reference.

Figure S6. Top: topography along profile A-A′ in Fig. 1. SAF: San Andreas Fault; GV: Great Valley. (bottom) CCP migration of the Ps phase using our preferred 2-D velocity model (Fig. S1). Green dots delineating the inferred slab and west dipping reflector structures from the CCP migration in Fig. 3 using the PpPp phase are shown for reference.

Figure S7. (top) Topography along profile A-A′ in Fig. 1. SAF: San Andreas Fault; GV: Great Valley. (bottom) CCP migration of the PpPs phase using our preferred 2-D velocity model (Fig. S1). Green dots delineating the inferred slab and west dipping reflector structures from the CCP migration in Fig. 3 using the PpPp phase are shown for reference.

Figure S8. (a) Seismic reflection profile across the mid-to-eastern Great Valley (GV) showing the base of the sediments and basin, along with a pair of subparallel west dipping reflectors (WDRs) at greater depth (see, e.g. Zoback & Wentworth 1986; Wentworth *et al.* 1987). (b) Map of reflection profile location (pink line) and CCSE stations (red dots). SAF: San Andreas Fault; SN: Sierra Nevada.

Figure S9. Top: topography along profile A-A′ in Fig. 1. SAF: San Andreas Fault. (bottom) Schematic cross-section overlaying the receiver function and Rayleigh wave tomography results. Green dots delineate the inferred slab and west dipping reflector structures from the CCP migration in Fig. 3. Projected locations of the 4.45 km/s (black dashed line) and 4.4 km s^{-1} (grey dashed line) *S*-wave velocity contours delineating the inferred slab from the Rayleigh wave tomography in Fig. 4 along profile A-A′ are shown for comparison. Note the lateral offset in the depicted location of the inferred slab between the receiver function and tomography results. GV: Great Valley basin.

Table S1. Event information for earthquakes used in the receiver function analysis from the Advanced National Seismic System (ANSS) Comprehensive Earthquake Catalog (ComCat).

Data Set S1. Event information for earthquakes used in Rayleigh wave tomography from the 1997–2009 International Seismological Centre Bulletin event catalogue (International Seismological Centre 2015) and the 2014–2015 ANSS ComCat event catalogue. Columns are origin time in YYYYMMDDHHMMSS format, longitude (degrees), latitude (degrees), depth (km), and magnitude (M_s).

Please note: Oxford University Press is not responsible for the content or functionality of any supporting materials supplied by the authors. Any queries (other than missing material) should be directed to the corresponding author for the paper.